

1 **Suppressed migrating diurnal tides in the MLT region during El**
2 **Niño in Northern Winter and its possible mechanism**

3 **Yetao Cen^{1,2,3}, Chengyun Yang^{1,2,3*}, Tao Li^{1,2,3*}, Jia Yue^{5,6}, James M. Russell III⁶,**
4 **and Xiankang Dou^{1,2,3,4}**

5 ¹CAS Key Laboratory of Geospace Environment, School of Earth and Space Sciences,
6 University of Science and Technology of China, Hefei, Anhui, China

7 ²Mengcheng National Geophysical Observatory, School of Earth and Space Sciences,
8 University of Science and Technology of China, Hefei, Anhui, China

9 ³CAS Center for Excellence in Comparative Planetology, University of Science and
10 Technology of China, Hefei, Anhui, China

11 ⁴School of Electronic Information, Wuhan University, Wuhan, Hubei, China

12 ⁵Catholic University of America, DC, USA

13 ⁶Center for Atmospheric Sciences, Hampton University, Hampton, VA, USA

14

15 Correspondence: Chengyun Yang (cyyang@ustc.edu.cn) and Tao Li

16 (litao@ustc.edu.cn)

Abstract

17

18 As observed by the Sounding of the Atmosphere using Broadband Emission
19 Radiometry (SABER), the migrating diurnal tide (DW1) in the upper mesosphere and
20 lower thermosphere (MLT) region decreased by $\sim 10\%$ during El Niño in the Northern
21 Hemisphere (NH) winter (December-January-February) from 2002 to 2020.
22 According to the multiple linear regression (MLR) analysis, the linear effects of El
23 Niño on the tropical MLT DW1 are significantly negative in both SABER
24 observations and SD-WACCM (the Specified-Dynamics version of the Whole
25 Atmosphere Community Climate Model) simulations. The DW1 response to El Niño
26 in NH winter is much stronger than its annual mean response. As suggested by
27 SD-WACCM simulation, Hough mode (1, 1) dominates the DW1 tidal variation in the
28 tropical MLT region. The consistency between the (1, 1) mode in the tropopause
29 region and the MLT region and the downward phase progression from 15 to 100 km
30 indicates the direct upward propagation of DW1 from the excitation source in the
31 troposphere. The suppressed DW1 heating rates in the tropical troposphere (averaged
32 over $\sim 0-16$ km and $35^{\circ}\text{S}-35^{\circ}\text{N}$) during El Niño winter contribute to the decreased
33 DW1 tide. To evaluate the effect of the gravity waves (GW) on the tide, the GW
34 forcing is calculated as the GW drag weighted by the phase relation between DW1
35 GW drag and DW1 wind. The negative GW forcing in the tropical upper mesosphere
36 would significantly suppress the MLT DW1 tide during El Niño winter. This tidal-GW
37 interaction could be a dominant mechanism for DW1 response in the MLT to El Niño.
38 During El Niño winter, the increased ratio of the absolute and planetary vorticity (R)
39 suppresses the waveguide and thus the DW1 amplitude in the subtropical mesosphere.
40 However, the effect of the waveguide might play a secondary role due to its relatively
41 weak response.

42 **1 Introduction**

43 Atmospheric solar tides are global-scale variations in meteorological variables
44 (e.g., density, wind, and temperature) with subharmonic periods of a solar day. The
45 migrating diurnal tide is dominant in the tropical mesosphere and lower thermosphere
46 (MLT) region and is characterized by westward traveling zonal wavenumber 1,
47 denoted as DW1 (Chapman & Lindzen, 1970). DW1 is primarily excited by the
48 absorption of infrared (IR) radiation by water vapor in the troposphere (~0–15 km)
49 (Hagan et al., 2002) and can propagate vertically and reach maximum amplitude in
50 the MLT region (Walterscheid., 1981a; McLandress et al., 1996; Liu & Hagan, 1998;
51 Lu et al., 2009; Liu et al., 2010; Yang et al., 2018). Diurnal migrating tides remain a
52 significant focus of scientific research due to a lack of comprehensive understanding
53 of their seasonal and interannual variabilities. The tidal variation in the MLT region
54 depends on variations in the wave sources, such as the solar heating absorption in the
55 lower atmosphere (Chapman & Lindzen, 1970), and the tidal wave propagation,
56 which is affected by background wind variation, such as the QBO (Forbes and
57 Vincent, 1989; Hagan et al., 1999; McLandress, 2002a; Ramesh et al., 2020;
58 McLandress, 2002b; Mayr and Mengel, 2005). In addition to tidal sources and
59 propagation, tidal variability is also affected by the modulation of interactions with
60 gravity waves (GW) (Liu and Hagan, 1998; Li et al., 2009).

61 As the dominant interannual variation in the tropical troposphere (Yulaeva and
62 Wallace, 1994), the El Niño-Southern Oscillation (ENSO), which is characterized by
63 anomalous sea surface temperature in the eastern equatorial Pacific Ocean, can cause
64 global-scale perturbations in atmospheric temperature, rainfall, and cloudiness and
65 potentially modulate tidal heating sources in the troposphere (Lieberman et al., 2007).
66 Previous studies have documented that ENSO can influence the troposphere (Yulaeva
67 and Wallace, 1994; Calvo-Fernandez et al., 2004) and the stratosphere and
68 mesosphere (Sassi et al., 2004; Randel et al., 2009; Li et al., 2013 and 2016). ENSO
69 events tend to reach their maximum in the Northern Hemisphere (NH) winter; they
70 could significantly impact the MLT tide.

71 According to meridional wind observations from the meteor radar at Jakarta
72 (6.4°S, 106.7°E) and medium-frequency (MF) radar at Tirunelveli (8.7°N, 77.8°E),
73 the tropical diurnal amplitudes in the meridional winds were suppressed during the El
74 Niño winters of 1994/1995 and 1997/1998 (Gurubaran et al., 2005). However,
75 Lieberman et al. (2007) documented a dramatic enhancement of the subtropical
76 diurnal tide in 1997 based on MF radar observations at Kauai, Hawaii (22°N, 154°W),
77 which may be connected to more substantial solar heating absorbed by water vapor
78 during the strong El Niño event of 1997-1998. Notably, the diurnal tidal amplitude
79 was only slightly enhanced during the winter of 1997/1998, when El Niño reached its
80 maximum. However, the diurnal tidal amplitudes were suppressed during the winters
81 of another 3 El Niño events (1991/1992, 1994/1995, and 2002/2003). Based on the
82 observations from ground-based radars and the Sounding of the Atmosphere using
83 Broadband Emission Radiometry (SABER) onboard the Thermosphere Ionosphere
84 Mesosphere Energetics and Dynamics (TIMED) satellite, Vitharana et al. (2021)
85 documented that the DW1 response to El Niño was negative from 2003 to 2016,
86 considering all the months. However, the response of DW1 to ENSO is different or
87 even opposite in different seasons, as suggested by previous studies (e.g., Lieberman
88 et al., 2007; Zhou et al., 2018; Kogure et al., 2021). For instance, Lieberman et al.
89 (2007) reported a dramatic enhancement of the subtropical diurnal tide during the
90 1997 autumn based on MF radar. From July to October of the strong El Niño of 2015,
91 the equatorial DW1 in the MLT was also dramatically enhanced in SABER (Zhou et
92 al., 2018; Kogure et al., 2021). Thus, calculating the regression by binning the data
93 among different months together may underestimate the actual response of MLT
94 DW1 tide in a particular season. Since ENSO reaches its peak in winter, more
95 pronounced effects in the upper atmosphere are expected. Thus, we focus on the
96 linear response of DW1 to ENSO during the winter in this study.

97 Utilizing the Whole Atmosphere Community Climate Model (WACCM) version
98 4, Pedatella & Liu (2012 and 2013) suggested that El Niño could enhance the MLT
99 DW1 tide during winters due to increased tropospheric radiative forcing. The QBO

100 signal is prescribed in WACCM4, and the ENSO events are self-generated. Based on
101 the WACCM version 6 simulations in which the QBO and ENSO are self-generated,
102 Ramesh et al. (2020) investigated the linear response of latitude-pressure variation of
103 DW1-T to the seven predictors, including ENSO in four seasons by adopting the
104 Multivariate linear regression. As suggested in Figure 5 by Ramesh et al. (2020), the
105 linear response of DW1 T amplitude to ENSO is significantly positive during the NH
106 winter in the tropical MLT region. However, Liu et al. (2017) found that DW1
107 amplitudes are suppressed during the winters of El Niño events based on simulations
108 of the ground-to-topside atmosphere-ionosphere for aeronomy (GAIA) model. Since
109 GAIA is nudged with reanalysis data below 30 km, ENSO events and variations in the
110 lower atmosphere are more realistic. The discrepancies among the model simulations
111 and uncertainties in the observations require further investigation of the DW1
112 tide-ENSO connection.

113 The response of the MLT DW1 tide to ENSO during the winters is revisited in
114 this study based on the DW1 variation extracted from a long-term temperature dataset
115 observed by the SABER onboard the TIMED satellite (Mertens et al., 2001 & 2004;
116 Rezac et al., 2015). The “Specified-Dynamics” version of the WACCM simulation is
117 used to study the possible mechanism. The data and methods are described in section
118 2. Section 3 presents the observational and model results of the DW1 temperature
119 response to ENSO. Section 4 examines the possible mechanism that modulates the
120 MLT DW1 tide during ENSO events. Finally, a summary is presented in section 5.

121

122 **2 Data and Methods**

123 The SABER began its observations in January 2002. Kinetic temperature profiles
124 are retrieved from the CO₂ limb emission profiles from the tropopause to the lower
125 thermosphere using a full non-LTE inversion (Mertens et al., 2001, 2004, Rezac et al.
126 2015). The latitude range of SABER observations is from 53° in one hemisphere to
127 83° in the other, and the latitude coverage flips to the opposite hemisphere

128 approximately every 60 days. Thus, SABER provides nearly continuous soundings
 129 within 53°S and 53°N. This study used version 2.0 temperature data from February
 130 2002 through July 2021 to analyze the DW1 temperature tide in the MLT region.
 131 SABER can complete a nearly 24-hr local time observation within a ~60-day window,
 132 allowing us to extract the diurnal tide explicitly.

133 The method described by Xu et al. (2007) is utilized to extract the DW1 tide
 134 from TIMED/SABER temperature data. Migrating tides can be expressed as

$$135 \quad \frac{1}{2\pi} \int_0^{2\pi} T(t_{LT}, \lambda) d\lambda = \bar{T}(t_{LT}) + \sum_{n=1}^N T_n^{mtw} \cos(n\omega_0 + \psi_n^{mtw}) + \varepsilon \quad (1)$$

136 where T is temperature, t_{LT} is local time, λ is longitude, overbar denotes zonal
 137 mean, the second term on the right side $\sum_{n=1}^N T_n^{mtw} \cos(n\omega_0 + \psi_n^{mtw})$ refers to
 138 migrating tides with $n = 1, 2, 3, 4$ corresponding to the diurnal, semidiurnal,
 139 terdiurnal and 6-h periods, T_n^{mtw} and ψ_n^{mtw} are the amplitude and phase of the
 140 migrating tide, and ε is the remnant of the temperature variability which could not be
 141 represented by the first two terms. The daily data are first divided into two groups
 142 according to their local time corresponding to the ascending and descending phases,
 143 respectively, to extract tidal components. Then, each group is interpolated into 12
 144 longitude grids, each 30° wide, by fitting with a cubic spline. The next step is to
 145 calculate the zonal mean for each day to eliminate the nonmigrating tides and the
 146 stationary planetary waves. The migrating tides' bimonthly amplitudes and phase
 147 information can be calculated by nonlinear least-squares fitting techniques using data
 148 within a 60-day sliding window every month (Xu et al., 2007; Smith et al., 2012; Gan
 149 et al., 2014).

150 The WACCM is a fully coupled chemistry-climate model, the high-top
 151 atmosphere component of the Community Earth System Model (CESM) (Garcia et al.,
 152 2007). In this study, the simulation of the Specified-Dynamics (SD) version of
 153 WACCM (SD-WACCM), version 4, is adopted to investigate the ENSO-DW1 tide
 154 relationship. The vertical range of SD-WACCM extends from the surface up to ~140
 155 km. The simulated diurnal tide in WACCM4 compares favorably with observations
 156 (Lu et al., 2011; Davis et al., 2013). SD-WACCM is nudged to meteorological fields

157 from Modern-Era Retrospective Analysis for Research and Applications (MERRA)
 158 reanalysis data in the troposphere and stratosphere (from the surface up to 1 hPa) and
 159 then is freely run in the MLT (above 0.3 hPa) (Kunz et al., 2011). Smith et al. (2017)
 160 discussed the dynamic constraints in SD-WACCM and their impact on the simulation
 161 of the mesosphere in detail. The ENSO-related characteristics in the troposphere and
 162 stratosphere in SD-WACCM follow those in the reanalysis meteorological fields with
 163 relaxation. In this study, the SD-WACCM output includes complete diurnal tidal
 164 information for temperature, zonal and meridional wind, and heating processes from
 165 1979 to 2014. The simulation also outputs the diurnal components of parameterized
 166 GW drag. We note here that the WACCM version 6 simulation was not used in this
 167 study due to its opposite response of MLT DW1 to ENSO compared to SABER
 168 observations.

169 The Niño3.4 index (N3.4), which is the sea surface temperature (SST) anomaly,
 170 averaged over 120°-170°W and 5°S-5°N (available at
 171 https://www.esrl.noaa.gov/psd/gcos_wgsp/Timeseries/Data/Niño34), is used to
 172 identify El Niño and La Niña events.

173 The monthly DW1 can be specified through its amplitude and phase. To evaluate
 174 the variations in both the amplitude and phase of the DW1 tide, the monthly DW1
 175 amplitudes are weighted by projecting the monthly mean vectors onto the
 176 climatological mean DW1 vector with the phase difference $\cos(\Delta\phi)$ (the phase
 177 difference is $\Delta\phi = \phi - \phi_{\text{clim}}$) as follows:

$$178 \quad \text{Amp}_{\text{weighted}} = \text{Amp} * \cos\left(\omega * (\phi - \phi_{\text{clim}})\right) \quad (2)$$

179 where ω ($\omega = 2\pi/24$) is the frequency of the DW1 tide. ϕ and ϕ_{clim} are the DW1
 180 phase of each month and the climatological mean, respectively. In the remainder of
 181 this study, the weighted DW1 amplitude (and its anomaly) refer to the DW1
 182 amplitude (anomaly) for conciseness. The mean tidal amplitude and phase during NH
 183 winter are derived from each year's averaged tidal vectors for December, January, and

184 February (DJF).

185 To derive the winter interannual variability that may be related to ENSO, we first
186 calculate the DW1 anomalies by removing the climatological mean seasonal cycle.
187 Then, the winter (DJF) mean of the DW1 anomalies is calculated. Natural forcing,
188 such as the solar cycle (represented by F107), QBO, ENSO, and long-term trends,
189 jointly affect the DW1 tidal amplitude (e.g., Dhady et al., 2018; Gurubaran et al.,
190 2005; Gurubaran & Rajaram, 1999; Hagan et al., 1999; Lieberman et al., 2007; Liu et
191 al., 2017; Pedatella & Liu, 2012; Sridharan, 2019, 2020; Sridharan et al., 2010;
192 Vincent et al., 1998; Xu et al., 2009). To isolate the linear forcing of ENSO from the
193 interference of other factors, a multivariate linear regression (MLR) analysis is
194 applied to the anomalous time series at each latitude and altitude, the same as that
195 used in Li et al. (2013).

$$196 \quad T(t) = C_1 * \text{Niño3.4} + C_2 * \text{QBO10} + C_3 * \text{QBO30} + C_4 * \text{F107} + C_5 * \\ 197 \quad \text{TREND} + \varepsilon(t) \quad (3)$$

198 where T is the DW1-T anomaly, t is time, C1–C5 are regression coefficients, and
199 ε is the residual; QBO10 and QBO30 are two orthogonal QBO time series derived
200 from the zonal wind (m s^{-1}) averaged over 5°N to 5°S at 10 and 30 hPa (Wallace et al.,
201 1993), respectively. The Niño3.4 index (Niño3.4) is the 3-month running mean of
202 SST averaged over 5°N to 5°S , 120°W - 170°W ; F107 is the solar radio flux at 10.7 cm,
203 which is a proxy for solar activity; and TREND is the long-term linear trend. The
204 linear contribution of each factor during winters is determined by applying MLR to
205 DJF anomalies each year. The analysis is carried out from 2002 to 2020 at each
206 latitude and pressure grid point. The F test (Kissell et al., 2017) was used to evaluate
207 the statistical significance of the regression coefficients.

208 The Hough function in classic tidal theory (Chapman & Lindzen, 1970), which
209 represents the solution of the Laplace tide equation in the isothermal atmosphere, can
210 set a consistent latitude variation in the amplitude and phase of the tidal perturbation
211 field. The Hough functions of daily variation frequency form a completely orthogonal
212 set and extend from 90°S to 90°N . This estimating amplitude and phase method is
213 based on fitting the Hough mode to the zonal structure representation and the simple

214 harmonic function (sine and cosine) to the local time-varying representation. The
 215 Hough mode is represented as $\Theta_{s,n}(\theta)$, or (s, n) , where s indicates the zonal
 216 wavenumber and index n is positive for gravitational modes (propagating modes) and
 217 negative for rotational modes (trapped modes). The normalized functions satisfy the
 218 following relation.

$$219 \quad \int_{-90^\circ}^{90^\circ} \Theta_{1,n}(\theta) \cdot \Theta_{1,m}(\theta) \cos(\theta) d\theta = \begin{cases} 1, & m = n \\ 0, & m \neq n \end{cases}, n, m = \pm 1, \pm 2, \dots \quad (4)$$

220

221 **3 Results**

222 As presented in Figure 1a, the NH winter (December-January-February, DJF)
 223 mean amplitude of DW1 in temperature extracted from TIMED/SABER observation
 224 is the largest (~12 K) in the equatorial mesopause region from 2002 to 2013.
 225 Although the amplitude is smaller, the distribution of the DW1 T amplitude in
 226 SD-WACCM simulation (Figure 1b) is similar to that derived from SABER
 227 observation, with the maximum at 90-100 km above the equator. There are some
 228 differences between SABER and SD-WACCM: SABER has a weaker peak above the
 229 equator at 70-80 km, but this peak cannot be seen in SD-WACCM.

230 Figures 2a and 2b show the monthly mean DW1 temperature amplitude
 231 anomalies (removing the climatological mean seasonal cycle) averaged over
 232 10°S-10°N at 100 km derived from SABER observations and SD-WACCM
 233 simulations between 2002 and 2020, respectively. Among the analyzed period, there
 234 were 4 El Niño events in 2002, 2006, 2009, and 2015, which are indicated with red
 235 arrows and defined by the Niño3.4 index in Figure 2c; the 3 La Niña events in 2007,
 236 2010, and 2020 are marked with blue arrows. The anomalous DW1 amplitudes are
 237 negative during 4 El Niño winters and positive during all 3 La Niña events. The DW1
 238 anomalies reach a positive maximum from July to October during the 2015/2016
 239 strong El Niño event, which agrees with Zhou et al. (2018); however, they become
 240 negative in winter. When SD-WACCM and SABER overlap (2002-2014), the

241 simulated DW1 amplitude anomalies in SD-WACCM are negative during all 3 El
242 Niño winters (2002, 2006, and 2009) and positive during 2 La Niña events. The
243 negative response of the MLT DW1 tide to El Niño in the SD-WACCM simulation
244 agrees well with that in the SABER observation.

245 In the 35-yr SD-WACCM simulations (1979-2014), the anomalous DW1
246 amplitudes averaged over 10°S-10°N at 100 km are negative during 7 of 8 El Niño
247 winters (1982, 1986, 1991, 1997, 2002, 2006, and 2009), as shown in Table 1. The
248 MLR coefficients of DW1 to normalized Niño3.4 are significantly negative in both
249 the SABER observation and SD-WACCM simulation, as shown in Figure 3. The
250 amplitude of DW1 in the equatorial region is reduced considerably. However, the
251 phase anomaly does not vary much (less than 1 hour) during El Niño winter. (Figures
252 S1, S2).

253 The MLT DW1 response to El Niño in winter is five times stronger than the
254 average response in SABER observations derived by Vitharana et al. (2021). This is
255 because the DW1 enhancement in El Niño autumn (e.g., Lieberman et al., 2007; Zhou
256 et al., 2018; Kogure et al., 2021) may weaken the negative response to ENSO. In the
257 simulations of Ramesh et al. (2020), different seasons also exhibit different responses
258 of DW1 to ENSO. The MLR coefficients of tropical DW1 to Niño3.4 in the SABER
259 observation (with a minimum of ~ -1 K/index) are twice as strong as those (with a
260 minimum of ~ -0.5 K/index) in the SD-WACCM simulation since the magnitude of
261 the DW1 tide is underestimated in the WACCM4 simulation (Liu et al., 2010; Lu et
262 al., 2012). The negative response of the MLT DW1-T amplitude to El Niño is
263 consistent with early MF radar/meteor radar observations and GAIA model
264 simulations with a nudging process (Gurubaran, 2005; Liu et al., 2017) but opposite to
265 free-run WACCM simulations (Pedatella & Liu, 2012 and 2013).

266 The MLR coefficients of the DW1 response to normalized QBO10 and QBO30
267 in the equatorial mesopause region are significantly positive, with a minimum of ~ 1
268 K/(m*s⁻¹) near 100 km (Figure S3), consistent with previous studies (Ramesh et al.

269 2020). The linear effects of the QBO on the MLT DW1 tides are comparable to those
270 of ENSO (the variances in the DW1 tide explained by ENSO, QBO10, and QBO30
271 are 23%, 20%, and 17%, respectively). The interaction between the QBO and ENSO
272 may potentially modulate the ENSO-DW1 tide relationship (Gray, 1984). In this study,
273 we focused on the linear effect of ENSO on the MLT DW1 tidal variability and the
274 associated mechanism. In SD-WACCM, the linear regression coefficients of DW1 are
275 a negative response to Niño3.4 and a positive response to QBO10 and QBO30, which
276 is consistent with the SABER observation. However, the absolute value of the
277 coefficients decreases more than that of SABER. The variance percentages of F107
278 are negligible compared with these three variables. In the remainder of this study,
279 only the linear effect of ENSO on the MLT DW1 tide is discussed.

280

281 **4 Possible Mechanisms**

282 **4.1 Tidal forcing and propagation**

283 A specific tidal component, such as DW1, can be decomposed into a series of
284 gravity wave-like modes and Rossby wave-like modes based on the Hough functions
285 (Figure S4) (Auclair-Desrotour et al., 2017; Chapman & Lindzen, 1970; Forbes,
286 1995). In a qualitative sense, the tidal response can be considered a combination of
287 GWs restored by stable stratification and inertial Rossby waves due to Coriolis
288 acceleration. The Hough modes of the DW1 tide in the SD-WACCM simulation are
289 analyzed to examine the mechanism of tropical DW1 tidal variation. As shown in
290 Figure 4a, the anomalies of the DW1 temperature amplitude averaged over 10°S-10°N
291 at 100 km are consistent with its Hough (1,1) component (the correlation coefficient
292 between MLT DW1-T anomalies and its Hough (1,1) component is 0.99) during the
293 NH winter from 1979 to 2013. The DW1-T amplitude anomalies and their Hough (1,1)
294 component during El Niño years decrease by 15% compared to the climatological
295 mean amplitude. During winters (DJF) from 1979 to 2013, the average phase of

296 DW1-T over 10°S-10°N shows general downward phase progression with the height
297 from the MLT region to the tropopause region (approximately 15 km), implying an
298 upward group velocity for the vertically propagating gravity wave model. By tracking
299 the downward phase progressive line, the altitude of the excitation source is estimated
300 to be below 15 km. The DW1-T phase during El Niño winters corresponds with the
301 climatological mean phase structure, implying that ENSO-induced tidal perturbation
302 in the troposphere could directly propagate vertically into the MLT region. The
303 anomalous Hough (1,1) mode of the DW1 temperature amplitude at MLT (100 km) is
304 significantly correlated (the correlation coefficient is 0.81) with that at the tropopause
305 region (15 km), indicating the effective propagation of the perturbation in the
306 tropospheric Hough (1,1) into the MLT region. During 7 of 8 El Niño events (1982,
307 1986, 1991, 1997, 2002, 2006, and 2009), the Hough (1,1) mode in the tropopause
308 decreased by approximately 15% compared to the climatological mean amplitude,
309 which agrees well with the anomalous Hough (1,1) in the MLT.

310 As noted earlier, the DW1 tide is primarily excited by the absorption of solar
311 radiation by tropospheric water vapor (Lieberman et al., 2003; Zhang et al., 2010).
312 According to the tidal theory (Volland, 1988), the heating rate of radiation absorbed
313 by water vapor in the entire troposphere is responsible for the excitation of diurnal
314 migrating tides. Next, we examine the perturbation of the DW1 solar heating source
315 in the SD-WACCM simulation, which potentially contributes to the negative Hough
316 (1,1) tidal anomalies in the tropopause region during El Niño winters. As presented in
317 Figure 5, the anomalous amplitudes of the DW1 heating rate (HR) regressed on the
318 normalized Niño3.4 index are significantly positive (with a maximum of ~ 0.4 mW/m³
319 per index) in the upper tropical troposphere (5°S-5°N, 3-12 km) but are significantly
320 negative below 3 km (with a minimum of ~ -4 mW/m³ per index). The ENSO-induced
321 changes in the tropospheric DW1 heating forcing may be due to the redistribution of
322 tropospheric convection during El Niño and La Niña winters. During El Niño winters,
323 increased moisture in the upper troposphere due to enhanced tropical precipitation in
324 the central Pacific Ocean (e.g., Hoerling et al., 1997) leads to stronger solar heating

325 absorption by water vapor in the middle and upper equatorial troposphere (5–12 km,
326 10°S–10°N).

327 On the other hand, heating in the lower troposphere significantly decreased due
328 to less solar radiation below the convective cloud. The DW1 HR regressed on
329 Niño3.4 in the NH (5°N–35°N) is characterized by a very negative coefficient of 3–8
330 km (with a maximum of ~ -0.3 mW/m³ per index) associated with significantly
331 positive coefficients below 2 km (with a maximum of ~ 3 mW/m³ per index). In the
332 Southern Hemisphere (SH), the distribution of DW1 HR coefficients consists of
333 negative and positive values at different altitudes and latitudes.

334 Pedatella et al. (2013) adopted the HR in the upper tropical troposphere (5–10 km
335 within $\pm 20^\circ$) to estimate the ENSO-induced variation in the DW1 tidal source. To
336 examine the excitation of the DW1 tide in the lower atmosphere, the HR averaged
337 over several different areas have been selected in previous studies (e.g., altitude range
338 between 900–200 hPa, 1–12 km in Lieberman et al., 2003, and 1000–100 hPa, 0–16 km
339 in Zhang et al., 2010). As suggested in Table 2, the mass-weighted HR averaged over
340 the entire tropical troposphere (0–16 km, 35°N–35°S), which negatively responds to
341 ENSO, is significantly correlated (the correlation coefficient is 0.45) with the DW1
342 tide in the tropical tropopause region. Although the linear regression coefficient in HR
343 is positive at 5–10 km over the equator (5°N–5°S), the coefficients at 5–30°N(S) are
344 negative (Figure 5), which is opposite of the equator (5°N–5°S). The HR averaged
345 over 5–10 km, 20°N–20°S (the same as in Pedatella et al., 2013) regressed on Niño3.4
346 is also negative, although it is not significantly correlated with the DW1 tidal
347 variation in the tropopause. The decreased DW1 heating source in the troposphere
348 during El Niño is a primary cause of the suppressed DW1 tide in the tropopause
349 region during winters, which propagates vertically and affects the DW1 tidal variation
350 in the MLT region.

351

352 4.2 Effect of background wind

353 The zonal wind in the middle atmosphere can modulate tide propagation from
354 the troposphere to the MLT (Forbes and Vincent, 1989). As McLandress (2002b)
355 described, the perturbation of latitudinal shear in the zonal mean zonal wind (zonal
356 mean vorticity) can affect DW1 propagation into the MLT region by causing
357 departures from classical tidal dynamics. The following equation gives the zonal
358 mean vorticity $\bar{\zeta}$ and Coriolis parameter f :

$$\bar{\zeta} = \frac{-1}{a \cos \theta} * \frac{\partial(\bar{u} \cos \theta)}{\partial \theta} \quad (5)$$

$$f = 2\Omega \sin \theta \quad (6)$$

$$R = (\bar{\zeta} + f)/f \quad (7)$$

359 where a , \bar{u} and θ correspond to the Earth radius, zonal mean zonal wind and
360 latitude, respectively, and Ω is the Earth's rotation rate.

361 The absolute and planetary vorticity R ratio is equivalent to changing the planet's
362 rotation rate. In classical theory, the vertically propagating DW1 is restricted near the
363 equator due to the planet's rapid rotation. Therefore, a faster rotation rate (positive R
364 anomalies) will suppress the latitudinal band (i.e., waveguide) where DW1 can
365 propagate vertically. On the other hand, the slower rotation rate (negative R anomalies)
366 favors the vertical propagation and is thus able to enhance the amplitude of DW1 at
367 low latitudes (McLandress, 2002b). When the ratio of the absolute and planetary
368 vorticity R -value at a certain height becomes larger, the upward propagation of tide is
369 suppressed, which leads to weaker tides above there.

370 The MLR coefficient of R on Niño3.4 is illustrated in Figure 6. Below 60 km,
371 the ratio R exhibits negative and positive responses to ENSO depending on different
372 altitudes in the Northern and Southern subtropics. The R response to ENSO is positive
373 at 60-100 km in the Northern subtropics and 65-100 km in the southern subtropics.

374 The green thick solid line represents the mean value of the equatorial R (15-30°N and
375 15-30°S), and it can be seen that the mean R-value response to ENSO is significantly
376 positive at 60-90 km. The increased ratio R in the mesosphere results in the
377 suppressed latitudinal band, which prevents the upward propagation of the DW1 tide
378 during El Niño winters. The correlation coefficient between the R-value and DW1
379 during the winter of 1979-2014 is ~ -0.33 in the SH and ~ -0.37 in the NH, implying
380 that the R plays a role in modulating the upward propagating of DW1 when no ENSO
381 event occurs. The variation of R and DW1 should not be attributed to the impacts of
382 ENSO separately.

383 **4.3 Effect of gravity wave forcing**

384 In addition to tidal sources and propagation, MLT tidal variability is also
385 affected by interactions with GWs (Liu and Hagan, 1998; Li et al., 2009). GWs are
386 the main driving force of MLT dynamic activity, which influences tidal amplitude and
387 phase (Walterscheid, 1981b; Lu et al., 2012; Liu et al., 2013). The effect of the GW
388 forcing on tides is not fully understood due to the limited observation and lack of
389 high-resolution model simulations that can fully resolve both tides and GWs. In
390 WACCM, the GWs are parameterized, and their tropical sources are interactive and
391 mainly triggered by convection in the tropics (Beres et al., 2005). The GW in the
392 tropics is primarily induced by convection, while the GW in the middle to high
393 latitudes is mainly generated by the frontal systems (Figure S5, S6). Due to this
394 interaction source, the GW drag will likely be modulated by ENSO as the location
395 and size of the ENSO-related convection change. The GW drag far away from the
396 tropospheric source strongly responds to the wind. As mentioned above, we can
397 determine the variation in the resistance of the convection-generated GW in the
398 WACCM. We mainly focus on the latitudinal component of parameterized resistance
399 because it is usually much larger than the meridional component (Yang et al., 2018).

400 In the NH winter, the DW1 GW drag caused by convection has apparent
401 hemispheric asymmetry: the magnitude is much smaller in the NH than in the SH

402 (Figure 7a). The zonal wind DW1 tide can be written as $U' = A^* \cos(\omega^*(t - \varphi) - s\lambda)$,
 403 where A and φ are the amplitude and phase of DW1 tide, ω ($\omega = 2\pi/24$) is DW1
 404 frequency, λ is longitude, and s ($s = 2\pi/360$) is the zonal wavenumber of DW1.
 405 The time tendency of the zonal wind can be written as
 406
$$\frac{\partial U'}{\partial t} = \omega^* A^* \cos(\omega^*(t - \varphi) + \frac{\pi}{2} - s\lambda) = \omega^* A^* \cos(\omega^*(t - (\varphi - 6)) - s\lambda); \quad (8)$$

407 The DW1 tide time tendency phase leads the tide itself by 6 hours. To evaluate the
 408 effect of GW forcing on the DW1 tide during DJF, the GW forcing can be calculated
 409 as $GW_{\text{forcing}} = GW_{\text{drag}}^* \cos(\omega^*(\varphi_{GW} - (\varphi_U - 6)))$; (9)

410 Where GW_{drag} is GW drag, and φ_{GW} and φ_U are the phase of DW1-GW and
 411 DW1-U.

412 The convection-generated GW forcing on the DW1 tide is positive in the
 413 southern subtropical upper mesosphere and negative below this tide (60–80 km)
 414 during the NH winter (Figure 7b). In the NH mesopause region, the GW forcing on
 415 the DW1 tide is positive in the subtropics (15–35°N) and negative in the tropics (0–10°
 416 N). This indicates that convection-generated GW forcing will dampen the tides in the
 417 tropical MLT and enhance the tides in the NH and SH subtropical regions (Figure 7b).
 418 As shown in Figure 8a, the correlation between DW1 U and GW drag from 1979 to
 419 2014 winter (DJF) is only significant in the mesopause region of southern subtropics
 420 and the equator. The correlation between DW1 U and GW forcing from 1979 to 2014
 421 winter (DJF) is more significant than 0.7 in the tropical and subtropical MLT (Figure
 422 8b). According to the F-test, the red areas indicate statistical significance above 95%,
 423 meaning GW forcing clearly modulates the tide, especially in the Southern subtropics.
 424 The linear regression coefficient of Niño3.4 in the GW forcing is significantly
 425 negative in the tropical MLT region (Figure 9, 80–100 km), suggesting that the

426 decreased GW forcing would lead to a weaker DW1 U amplitude during El Niño
427 winters.

428 Although parameterized GWs are excited by convection (in the tropics), it is
429 difficult to find a direct cause and effect relationship between ENSO-related
430 tropospheric changes and the GW-induced tidal forcing in the mesosphere. The GW
431 forcing in the MLT not only depends on the generation of waves in the troposphere
432 but also on zonal wind filtering when they propagate upward from the troposphere to
433 the upper mesosphere. However, our study suggests that the ENSO modulation of
434 tidal amplitude can come from the disturbance in tropospheric tidal sources, tidal
435 propagation modulated by zonal wind, and the disturbance of the GW-tidal interaction
436 in the upper mesosphere.

437

438 **5 Discussion and Summary**

439 The response of the MLT DW1 tide to ENSO is investigated during the Northern
440 winter when ENSO reaches its peak by using satellite observations of temperature
441 profiles and the SD-WACCM simulation. The DW1 temperature amplitude observed
442 by SABER tends to decrease during the NH winter of 4 El Niño events between 2002
443 and 2020 when El Niño reaches its peak and increases during 3 La Niña events. In
444 SD-WACCM simulations, the DW1 amplitude is suppressed during 7 of 8 El Niño
445 winter (DJF) events from 1979 to 2014.

446 Possible mechanisms have been proposed to explain the DW1 response to ENSO:
447 (1) the source of tidal excitation in the lower atmosphere and its upward propagation,
448 (2) the impact of background wind variation on the tidal propagation, and (3)
449 interaction between gravity waves and tides. As the Hough (1,1) mode dominates the
450 diurnal migrating tidal temperature in the MLT region, its negative response to ENSO
451 corresponds well with the counterpart at the tropopause. By tracking the downward
452 phase progressive line, the altitude of the excitation source is estimated to be below

453 15 km. The decreased heating rate in the tropical troposphere (35°S-35°N, 0-16 km)
454 during El Niño contributes to the suppressed DW1 tidal amplitude in the tropical
455 tropopause.

456 As the background variation could modulate the upward propagation of the tide
457 (Forbes and Vincent, 1989; McLandress, 2002a, 2002b), the ratio of the absolute and
458 planetary vorticity R response to ENSO is investigated. The R response to ENSO is
459 significantly positive at 60-90 km, leading to the narrower waveguide and resulting in
460 weaker DW1 amplitude above. However, the regression coefficient of R on the ENSO
461 index is relatively small compared to the mean value of R , which implies that the
462 impact of R on tidal propagation may play a secondary role in the ENSO-DW1
463 connection.

464 In addition to tidal sources and propagation, MLT tidal variability is also
465 dramatically affected by interactions with GWs (Liu and Hagan, 1998; Li et al., 2009).
466 GW forcing considering both the DW1 tidal GWs drag and the phase difference with
467 the DW1 tide is calculated to evaluate the effect of the GW variation on the tide
468 during ENSO winters. The GW forcing response to Niño3.4 is significantly negative
469 in the tropical upper mesosphere, which suggests the GW response to ENSO tends to
470 dampen the MLT DW1 tide during El Niño winter. This tidal-GW interaction could
471 significantly modulate the tidal amplitude, as revealed by early lidar observations (Li
472 et al., 2009; Baumgarten et al., 2018). This could be the most important mechanism of
473 DW1 response in the MLT region to ENSO. However, quantitative evaluation of this
474 interaction is out of the scope of this paper and needs a far more sophisticated model
475 with extremely high resolution to self-generate convective GWs.

476 The weak negative DW1 response to ENSO over the equator may be related to
477 the dissipation or damping of the tide near 95 km. The shorter vertical wavelength
478 would increase the Rayleigh friction coefficient (Forbes et al., 1989), enhancing the
479 tide dissipation. As presented in Table S1, the vertical wavelength of DW1 near 95
480 km is increased (but decreased at around 90 and 100 km), which would suppress the

481 Rayleigh friction coefficient and lead to less tidal dissipation. Therefore, the less tidal
482 dissipation in this area could result in a relatively weak negative or even positive
483 response to ENSO near 95 km. The interaction of gravity waves and tides may also
484 play a role in modulating the tidal amplitude at different altitudes. However, the
485 SD-WACCM simulation failed to perform a similar tidal response near 95 km as
486 SABER observations. Further investigation is needed with more detailed GW
487 observations or the improved GW parameterization scheme and higher vertical
488 resolution in the model simulation.

489 **Data availability**

490 SABER datasets are available at <http://saber.gats-inc.com/data.php>, and
491 SD-WACCM datasets used here are obtained at
492 <http://doi.org/10.6084/m9.figshare.19777918>.

493

494 **Author contributions**

495 YC and CY designed the study, performed data analysis, prepared the figures,
496 and wrote the manuscript. TL initiated the research and contributed to supervision and
497 interpretation. JY and JR contributed to editing the manuscript. XD contributed to the
498 interpretation. All authors contributed to the discussion and interpretation.

499

500 **Competing interests**

501 The authors declare that they have no conflict of interest.

502

503 **Acknowledgments**

504 This work was supported by the National Natural Science Foundation of China
505 grants (42130203, 41874180, 41974175), the B-type Strategic Priority Program of the

506 Chinese Academy of Sciences, Grant No. XDB41000000, and the pre-research
507 project on Civil Aerospace Technologies No. D020105 funded by China's National
508 Space Administration. JY and JMR's work is supported by the National Science
509 Foundation grant AGS-1901126.

510 **Reference**

- 511 Auclair-Desrotour, P., Laskar, J., and Mathis, S.: Atmospheric tides and their
512 consequences on the rotational dynamics of terrestrial planets.
513 EAS Publications Series, 82 (2019) 81-90,
514 <https://doi.org/10.1051/eas/1982008>, 2017.
- 515 Baumgarten, K., Gerding, M., Baumgarten G., and Luebken, F. J.: Temporal
516 variability of tidal and gravity waves during a record long 10-day continuous
517 lidar sounding. *Atmospheric chemistry and physics*, 18, 371-384,
518 <https://doi.org/10.5194/acp-18-371-2018>, 2018
- 519 Beres, J. H., Garcia, R. R., Boville, B. A., and Sassi, F.: Implementation of a gravity
520 wave source spectrum parameterization dependent on the properties of
521 convection in the Whole Atmosphere Community Climate Model (WACCM).
522 *Journal of Geophysical Research*, 110, D10108,
523 <https://doi.org/10.1029/2004JD005504>, 2015.
- 524 Calvo-Fernández, N., Herrera, R. G., Puyol, D. G. , Martín, E. H., García, R. R., Presa,
525 L. G., and Rodrlguez, P. R.: Analysis of the enso signal in tropospheric and
526 stratospheric temperatures observed by MSU, 1979-2000. *Journal of*
527 *Climate*, 17(20), 3934-3946,
528 [http://doi.org/10.1175/1520-0442\(2004\)017<3934:aotesi>2.0.co;2](http://doi.org/10.1175/1520-0442(2004)017<3934:aotesi>2.0.co;2), 2004.
- 529 Chapman, S., and Lindzen, R. S.: *Atmospheric Tides*, 201 pp., D. Reidel, Norwell,
530 Mass., 1970.
- 531 Davis, R. N., Du, J., Smith, A. K., Ward, W. E., and Mitchell, N. J.: The diurnal and
532 semidiurnal tides over Ascension Island (8°S, 14°W) and their interaction with
533 the stratospheric QBO: Studies with meteor radar, eCMAM and WACCM.
534 *Atmospheric Chemistry and Physics*, 13(18), 9543–9564,
535 <https://doi.org/10.5194/acp-13-9543-2013>, 2013.
- 536 Dhadly, M. S., Emmert, J. T., Drob, D. P., McCormack, J. P., and Niciejewski, R.:
537 Short-term and interannual variations of migrating diurnal and semidiurnal tides
538 in the mesosphere and lower thermosphere. *Journal of Geophysical Research:*
539 *Space Physics*, 123, 7106–7123, <https://doi.org/10.1029/2018JA025748>, 2018.

540 Forbes, J. M.: Tidal and planetary waves. *Geophysical Monograph Series*, 87,
541 <https://doi.org/10.1029/GM087p0067>, 1995.

542 Forbes, J. M., and Vincent, R. A.: Effects of mean winds and dissipation on the
543 diurnal propagating tide: an analytic approach. *Planetary & Space Science*, 37(2),
544 197-209, [https://doi.org/10.1016/0032-0633\(89\)90007-X](https://doi.org/10.1016/0032-0633(89)90007-X), 1989.

545 Gan, Q., Du, J., Ward, W. E., Beagley, S. R., Fomichev, V. I., and Zhang, S.:
546 Climatology of the diurnal tides from eCMAM30 (1979 to 2010) and its
547 comparisons with SABER. *Earth Planets Space* 66:103,
548 <https://doi.org/10.1186/1880-5981-66-103>, 2014.

549 Garcia, R. R., Marsh, D. R., Kinnison, D. E., Boville, B. A., and Sassi, F.: Simulation
550 of secular trends in the middle atmosphere, 1950-2003. *Journal of Geophysical*
551 *Research*, 112, D09301, <https://doi.org/10.1029/2006JD007485>, 2007.

552 Gray, W. M.: Atlantic seasonal hurricane frequency: Part I: El Niño and 30 mb
553 quasi-biennial oscillation influences. *Mon. Wea. Rev.*, 112, 1649–1668,
554 [https://doi.org/10.1175/1520-0493\(1984\)112<1649:ASHFPI>2.0.CO;2](https://doi.org/10.1175/1520-0493(1984)112<1649:ASHFPI>2.0.CO;2), 1984.

555 Gurubaran, S., and Rajaram, R.: Long-term variability in the mesospheric tidal winds
556 observed by MF radar over Tirunelveli (8.7°N, 77.8°E). *Geophysical Research*
557 *Letters*, 26(8), 1113–1116, <https://doi.org/10.1029/1999GL900171>, 1999.

558 Gurubaran, S., Rajaram, R., Nakamura, T., and Tsuda, T.: Interannual variability of
559 diurnal tide in the tropical mesopause region: a signature of the El Niño-Southern
560 Oscillation (ENSO). *Geophysical Research Letters* 32(13),
561 <https://doi.org/10.1029/2005gl022928>, 2005.

562 Hagan, M. E., Burrage, M. D., Forbes, J. M., Hackney, J., Randel, W. J., and Zhang,
563 X.: QBO effects on the diurnal tide in the upper atmosphere. *Earth Planet Space*,
564 51, 571–578, <http://doi.org/10.1186/BF03353216>, 1999.

565 Hagan, M. E., and Forbes, J. M.: Migrating and nonmigrating diurnal tides in the
566 middle and upper atmosphere excited by tropospheric latent heat release, *J.*
567 *Geophys. Res.*, 107(D24), 4754, <https://doi.org/10.1029/2001JD001236>, 2002.

568 Hoerling, M. P., Kumar A., and Zhong. M.: El Niño, La Niña, and the nonlinearity of
569 their teleconnections, *Journal of Climate*, 10, 1769-1786,
570 [https://doi.org/10.1175/1520-0442\(1997\)010<1769:ENOLNA>2.0.CO;2](https://doi.org/10.1175/1520-0442(1997)010<1769:ENOLNA>2.0.CO;2), 1997.

571 Kissell, R., and Poserina, J.: Optimal Sports Math, Statistics, and Fantasy,
572 <https://doi.org/10.1016/B978-0-12-805163-4.00002-5>, 2017.

573 Kogure, M., and Liu, H.: DW1 tidal enhancements in the equatorial MLT during 2015
574 El Niño: The relative role of tidal heating and propagation. *Journal of*
575 *Geophysical Research: Space Physics*, 126, e2021JA029342,
576 <https://doi.org/10.1029/2021JA029342>, 2021.

577 Kunz, A., Pan, L., Konopka, P., Kinnison, D., and Tilmes, S.: Chemical and
578 dynamical discontinuity at the extratropical tropopause based on START08 and
579 WACCM analyses. *Journal of Geophysical Research*, 116, D24302,
580 <https://doi.org/10.1029/2011JD016686>, 2011.

581 Lieberman, R. S., Ortland, D. A., and Yarosh, E. S.: Climatology and interannual
582 variability of diurnal water vapor heating. *Journal of Geophysical Research:*
583 *Atmospheres* 108(D3), <https://doi.org/10.1029/2002jd002308>, 2003.

584 Lieberman, R. S., Riggin, D. M., Ortland, D. A., Nesbitt, S. W., and Vincent, R. A.:
585 Variability of mesospheric diurnal tides and tropospheric diurnal heating during
586 1997–1998. *Journal of Geophysical Research: Atmospheres* 112(D20),
587 <https://doi.org/10.1029/2007jd008578>, 2007.

588 Li, T., She, C. Y., Liu, H., Yue, J., Nakamura, T., Krueger, D. A.: Observation of
589 local tidal variability and instability, along with dissipation of diurnal tidal
590 harmonics in the mesopause region over Fort Collins, Colorado (41°N, 105°W).
591 *Journal of Geophysical Research: Atmospheres* (1984–2012), 114(D6),
592 <https://doi.org/10.1029/2008jd011089>, 2009.

593 Li, T., Calvo, N., Yue, J., Dou, X., Russell III, J. M., Mlynczak, M. G., She, C. Y.,
594 and Xue, X.: Influence of El Niño–Southern Oscillation in the mesosphere.
595 *Geophysical Research Letters*, 40, 3292–3296, <https://doi.org/10.1002/grl.50598>,
596 2013.

597 Li, T., Calvo, N., Yue, J., Russell III, J. M., Smith, A. K., Mlynczak, M. G., Chandran,
598 A., Dou, X., and Liu, A. Z.: Southern Hemisphere summer mesopause responses
599 to El Niño-Southern Oscillation. *Journal of Climate*, 29(17),
600 6319– 6328, <https://DOI.org/10.1175/JCLI-D-15-0816.1>, 2016.

601 Liu, A. Z., Lu, X., and Franke, S. J.: Diurnal variation of gravity wave momentum
602 flux and its forcing on the diurnal tide. *Journal of Geophysical Research –*
603 *Atmospheres*, 118, 1668–1678, <https://doi.org/10.1029/2012JD018653>, 2013.

604 Liu, H., Sun, Y. Y., Miyoshi, Y., and Jin, H.: ENSO effects on MLT diurnal tides: A
605 21 year reanalysis data-driven GAIA model simulation. *Journal of Geophysical*
606 *Research: Space Physics*, 122, 5539-5549,
607 <https://doi.org/10.1002/2017JA024011>, 2017.

608 Liu, H. L., Wang, W., Richmond, A. D., and Roble, R. G.: Ionospheric variability due
609 to planetary waves and tides for solar minimum conditions. *Journal of*
610 *Geophysical Research: Space Physics*, 115, A00G01,
611 <https://doi.org/10.1029/2009JA015188>, 2010.

612 Liu, H. L., and Hagan, M. E.: Local heating/cooling of the mesosphere due to gravity
613 wave and tidal coupling. *Geophysical Research Letters*, 25, 2941–2944,
614 <https://doi.org/10.1029/98GL02153>, 1998.

615 Lu, X., Liu, A. Z., Swenson, G. R., Li, T., Leblanc, T., and McDermid, I. S.: Gravity
616 wave propagation and dissipation from the stratosphere to the lower
617 thermosphere. *Journal of Geophysical Research: Atmospheres*, 114, D11101,
618 <https://doi.org/10.1029/2008JD010112>, 2009.

619 Lu, X., Liu, H. L., Liu, A. Z., Yue, J., McInerney, J. M., and Li, Z.: Momentum
620 budget of the migrating diurnal tide in the Whole Atmosphere Community
621 Climate Model at vernal equinox. *Journal of Geophysical Research*, 117,
622 D07112, <https://doi.org/10.1029/2011JD017089>, 2012.

623 Lu, X., Liu, A. Z., Oberheide, J., Wu, Q., Li, T., Li, Z., ... and Franke, S. J.: Seasonal
624 variability of the diurnal tide in the mesosphere and lower thermosphere over
625 Maui, Hawaii (20.7°N, 156.3°W). *Journal of Geophysical Research*, 116,
626 D17103, <https://doi.org/10.1029/2011JD015599>, 2011.

627 Mayr H. G., and Mengel J. G.: Interannual variations of the diurnal tide in the
628 mesosphere generated by the quasi-biennial oscillation, *J Geophys Res*
629 110:D10111, <http://doi.org/10.1029/2004JD005055>, 2005.

630 McLandress, C., Shepherd, G. G., and Solheim, B. H.: Satellite observations of
631 thermospheric tides: Results from the wind imaging interferometer on UARS.
632 *Journal of Geophysical Research: Atmospheres* 101(D2):4093–4114,
633 <https://doi.org/10.1029/95jd03359>, 1996.

634 McLandress, C.: Interannual variations of the diurnal tide in the mesosphere induced
635 by a zonal- mean wind oscillation in the tropics, *Geophys. Res. Lett.*, 29(9),
636 <http://doi.org/10.1029/2001GL014551>, 2002a.

637 McLandress, C.: The seasonal variation of the propagating diurnal tide in the
638 mesosphere and lower thermosphere. Part II: The role of tidal heating and zonal
639 mean winds, *J. Atmos. Sci.*, 59(5), 907–922,
640 [https://doi.org/10.1175/1520-0469\(2002\)059<0907:Tsvotp>2.0.Co;2](https://doi.org/10.1175/1520-0469(2002)059<0907:Tsvotp>2.0.Co;2), 2002b.

641 Mertens, C. J., Mlynczak, M. G., Lopez-Puertas, M., Wintersteiner, P. P., Picard, R.
642 H., Winick, J. R., and Gordley, L. L.: Retrieval of mesospheric and lower
643 thermospheric kinetic temperature from measurements of CO₂ 15 μm Earth
644 limb emission under non-LTE conditions, *Geophysical Research Letters*, 28(7),
645 1391-1394, <https://doi.org/10.1029/2000GL012189>, 2001.

646 Mertens, C. J., Schmidlin, F. J., Goldberg, R. A., Remsberg, E. E., Pesnell, W. D.,
647 Russell, J. M., Mlynczak, M. G., Lopez-Puertas, M., Wintersteiner, P. P., Picard,
648 R. H., Winick, J. R., and Gordley, L. L.: SABER observations of mesospheric
649 temperatures and comparisons with falling sphere measurements taken during
650 the 2002 summer MaCWAVE campaign. *Geophysical Research Letters* 31(3),
651 <https://doi.org/10.1029/2003gl018605>, 2004.

652 Pedatella, N. M., and Liu, H. L.: Tidal variability in the mesosphere and lower
653 thermosphere due to the El Niño-Southern Oscillation. *Geophysical Research*
654 *Letters* 39, <https://doi.org/10.1029/2012gl053383>, 2012.

655 Pedatella, N. M., and Liu, H. L.: Influence of the El Niño Southern Oscillation on the
656 middle and upper atmosphere. *Journal of Geophysical Research: Atmospheres*
657 118(5):2744–2755, <https://doi.org/10.1002/Jgra.50286>, 2013.

658 Ramesh, K., Smith, A. K., Garcia, R. R., Marsh, D. R., Sridharan, S., and Kishore
659 Kumar, K.: Long-term variability and tendencies in migrating diurnal tide from
660 WACCM6 simulations during 1850–2014. *Journal of Geophysical Research:*
661 *Atmospheres*, 125, e2020JD033644, <https://doi.org/10.1029/2020JD033644>,
662 2020.

663 Randel, W. J. , Shine, K. P. , Austin, J. , Barnett, J. , Claud, C. , and Gillett, N. P.: An
664 update of observed stratospheric temperature trends. *Journal of Geophysical*
665 *Research: Atmospheres*. 114, D02107, <https://doi.org/10.1029/2008JD010421>,
666 2009.

667 Rezac, L., Jian, Y., Yue, J., Russell III, M. J., Kutepov, A., Garcia, R., Walker, K.,
668 and Bernath, P.: Validation of the global distribution of CO₂ volume mixing
669 ratio in the mesosphere and lower thermosphere from SABER, *J. Geophys. Res.*
670 *Atmos.*, 120, 12,067-12,081,
671 <https://doi.org/10.1002/2015JD023955>, 2015.

672 Sassi, F., Kinnison, D., Boville, B., Garcia, R., and Roble, R.: Effect of el
673 niño–southern oscillation on the dynamical, thermal, and chemical structure of
674 the middle atmosphere. *Journal of Geophysical Research*, 109(D17), D17108,
675 <http://doi.org/10.1029/2003jd004434>, 2004.

676 Smith, A. K.: Global Dynamics of the MLT. *Surveys in Geophysics*, 33(6):
677 1177-1230, <https://doi.org/10.1007/s10712-012-9196-9>, 2012.

678 Smith, A. K., Pedatella, N. M., Marsh, D. R., and Matsuo, T.: On the Dynamical
679 Control of the Mesosphere–Lower Thermosphere by the Lower and Middle
680 Atmosphere, *Journal of the Atmospheric Sciences*, 74(3), 933-947,
681 <https://doi.org/10.1175/JAS-D-16-0226.1>, 2017.

682 Sridharan, S., Tsuda, T., and Gurubaran, S.: Long-term tendencies in the
683 mesosphere/lower thermosphere mean winds and tides as observed by
684 medium-frequency radar at Tirunelveli (8.7° N, 77.8° E). *Journal of Geophysical*

685 Research: Atmospheres, 115(D8),
686 <http://doi.org/10.1029/2008JD011609>, 2010.

687 Sridharan, S.: Seasonal variations of low-latitude migrating and nonmigrating diurnal
688 and semidiurnal tides in TIMED-SABER temperature and their relationship with
689 source variations. *Journal of Geophysical Research: Space Physics*, 124,
690 3558–3572,
691 <https://doi.org/10.1029/2018JA026190>, 2019.

692 Sridharan, S.: Equatorial upper mesospheric mean winds and tidal response to strong
693 El Niño and La Niña. *Journal of Atmospheric and Solar-Terrestrial Physics*, 202,
694 105270,
695 <https://doi.org/10.1016/j.jastp.2020.105270>, 2020.

696 Vincent, R. A., Kovalam, S., Fritts, D. C., & Isler, J. R.: Long-term MF radar
697 observations of solar tides in the low-latitude mesosphere: Interannual variability
698 and comparisons with GSWM. *Journal of Geophysical Research*, 103(D8),
699 8667–8683, <https://doi.org/10.1029/98JD00482>, 1998.

700 Vitharana, A., Du, J., Zhu, X., Oberheide, J., and Ward, W. E.: Numerical prediction
701 of the migrating diurnal tide total variability in the mesosphere and lower
702 thermosphere. *Journal of Geophysical Research: Space Physics*, 126,
703 e2021JA029588, <https://doi.org/10.1029/2021JA029588>, 2021.

704 Volland, H.: *Atmospheric Tidal and Planetary Waves*[M]. Springer Netherlands,
705 1988.

706 Wallace, J. M., Panetta, R. L., and Estberg J.: Representation of the equatorial
707 quasi-biennial oscillation in EOF phase space. *Journal of the Atmospheric*
708 *Sciences*, 50, 1751-1762,
709 [https://doi.org/10.1175/1520-0469\(1993\)050<1751:ROTESQ>2.0.CO;2](https://doi.org/10.1175/1520-0469(1993)050<1751:ROTESQ>2.0.CO;2), 1993.

710 Walterscheid, R. L.: Inertia-gravity wave induced accelerations of mean flow having
711 an imposed periodic component: Implications for tidal observations in the meteor
712 region. *Journal of Geophysical Research: Atmospheres*, 86, 9698-9706,
713 <https://doi.org/10.1029/JC086iC10p09698>, 1981a.

714 Walterscheid, R. L.: Dynamical cooling induced by dissipating internal gravity waves.
715 Geophysical Research Letters, 8(12), 1235-1238,
716 <https://doi.org/10.1029/GL008i012-p01235>, 1981b.

717 Xu, J. Y., Liu, H. L., Yuan, W., Smith, A. K., Roble, R. G., Mertens, C. J., Russell, J.
718 M., and Mlynczak, M. G.: Mesopause structure from thermosphere, ionosphere,
719 mesosphere, energetics, and dynamics (TIMED)/sounding of the atmosphere
720 using broadband emission radiometry (SABER) observations. Journal of
721 Geophysical Research: Atmospheres 112 (D9),
722 <https://doi.org/10.1029/2006jd007711>, 2007a.

723 Xu, J. Y., Smith, A. K., Yuan, W., Liu, H. L., Wu, Q., Mlynczak, M. G., and Russell,
724 J. M.: Global structure and long-term variations of zonal mean temperature
725 observed by TIMED/SABER. Journal of Geophysical Research: Atmospheres,
726 112, D24106, <https://doi.org/10.1029/2007jd008546>, 2007b.

727 Xu, J., Smith, A. K., Liu, H.-L., Yuan, W., Wu, Q., Jiang, G., Mlynczak, G. M.,
728 Russell III, J. M., and Franke, S. J.: Seasonal and quasi-biennial variations in the
729 migrating diurnal tide observed by Thermosphere, Ionosphere, Mesosphere,
730 Energetics and Dynamics (TIMED), J. Geophys. Res., 114, D13107,
731 <https://doi.org/10.1029/2008JD011298>, 2009.

732 Yang, C., Smith, A. K., Li, T., and Dou, X.: The effect of the Madden-Julian
733 oscillation on the mesospheric migrating diurnal tide: A study using
734 SD-WACCM. Geophysical Research Letters, 45, 5105-5114,
735 <https://doi.org/10.1029/2018GL077956>, 2018.

736 Yulaeva, E., & Wallace, J. M.: The signature of ENSO in global temperature and
737 precipitation fields derived from the microwave sounding unit. Journal of
738 climate, 7(11), 1719-1736,
739 [https://doi.org/10.1175/1520-0442\(1994\)007<1719:TSEOIG>2.0.CO;2](https://doi.org/10.1175/1520-0442(1994)007<1719:TSEOIG>2.0.CO;2), 1994.

740 Zhang, X., Forbes, J. M., and Hagan, M. E.: Longitudinal variation of tides in the
741 MLT region: 1. Tides driven by tropospheric net radiative heating. Journal of
742 Geophysical Research: Space Physics, 115, A06316,
743 <https://doi.org/10.1029/2009JA014897>, 2010.

744 Zhou, X., Wan, W., Yu, Y., Ning, B., Hu, L., and Yue, X.: New approach to estimate
745 tidal climatology from ground-and space-based observations. Journal of
746 Geophysical Research: Space Physics, 123, 5087-5101,
747 <http://doi.org/10.1029/2017JA024967>, 2018.

748

749

750 **Table 1.** The list of ENSO years with corresponding Niño3.4 indices and anomaly DWI
 751 temperature amplitudes of the SD-WACCM simulations averaged over 10°S-10°N at 100 km.

El Niño events	Niño3.4 index	SD-WACCM anomalous DWI T AMP (K)
1982-1983	2.14	-0.22
1986-1987	1.11	-2.90
1991-1992	1.69	-1.56
1994-1995	1.22	1.56
1997-1998	2.33	-1.87
2002-2003	1.37	-0.55
2006-2007	1.09	-1.30
2009-2010	1.43	-1.82
AVG	1.54	-0.96

752

753

754 **Table 2.** The correlation coefficient between the DWI T amplitude at 15 km and the
 755 mass-weighted HR in different areas during the winters of 1979-2014. The bold numbers indicate
 756 that the correlation coefficients are significant at 95%. The MLR coefficient on the normalized
 757 Niño3.4 index ($10^{-3} \text{ mw m}^{-3} \text{ index}^{-1}$) is also exhibited.

Altitude and latitude ranges	0-16 km, 35°N-35°S	0-12 km, 35°N-35°S	5-10 km, 35°N-35°S	5-10 km, 20°N-20°S
Correlation coefficient	0.45	0.36	0.32	0.32
MLR coefficient on Niño3.4	-3	-10	-26	-9

758

759 **Figure captions**

760 **Figure 1.** (a) The average DW1 temperature amplitude of SABER observation during the
761 2002-2013 winter (DJF, Dec-Jan-Feb). (b) the same as (a), but for SD-WACCM.

762 **Figure 2.** (a) The residual DW1 temperature amplitude of SABER observations averaged over
763 10°S-10°N at 100 km from 2002 to 2021. (b) Same as in (a) but for SD-WACCM. (c) Niño3.4
764 index. Dashed lines represent ENSO events. The red solid and hollow blue arrows denote the El
765 Niño and La Niña events.

766 **Figure 3.** The linear regression coefficient of normalized Niño3.4 in SABER (a) and SD-WACCM
767 (b) winter DW1-T. The contour interval is 0.2 K for SABER and 0.1 K for SD-WACCM. Solid
768 lines and red shadings denote the positive responses, while dashed lines and blue shadings denote
769 the negative responses; the grey regions indicate where the response is insignificant at the 95%
770 level according to the F test.

771 **Figure 4.** (a) The solid red line indicates the anomalous DW1 temperature amplitude of
772 SD-WACCM simulations averaged over 10°S-10°N at 100 km during the 1979-2013 winter (DJF).
773 The blue dotted line indicates the Hough (1,1) mode of the DW1 temperature amplitude residual at
774 100 km during the 1979-2013 winter (DJF). (b) The thin black dotted line indicates the Hough
775 (1,1) DW1-T phase of SD-WACCM simulations at 0-100 km during the 1979-2013 winter (DJF).
776 The thick black horizontal line indicates the standard deviation of the DW1-T phase. The solid red
777 line is the same but for El Niño winter. (c) The solid blue line is the same as in (a), and the black
778 dotted line is the same but for 15 km.

779 **Figure 5.** The linear regression coefficient of normalized Niño3.4 in SD-WACCM heating
780 amplitude (mW/m^3 per index) during 1979-2013 winters (DJF). Solid lines and red shadings
781 denote the positive responses, while dashed lines and blue shadings denote the negative responses;
782 the grey regions indicate where the response is insignificant at the 95% level according to the F
783 test.

784 **Figure 6.** The linear regression coefficient of normalized Niño3.4 in δR (the anomaly of the ratio
785 of the absolute to planetary vorticity). The thin dashed red, blue, and green lines denote the
786 averages of the Northern Hemisphere (from 15°N to 30°N), Southern Hemisphere (from 15°S to
787 30°S), and the whole (15-30°N and 15-30°S), respectively. The thick, solid lines denote

788 confidence levels higher than 95% for the F test.

789 **Figure 7.** (a) Gravity Wave (GW) drag due to convection on the amplitude of DW1 tidal U during
790 the winter (DJF). (b) The same as (a), but for GW forcing.

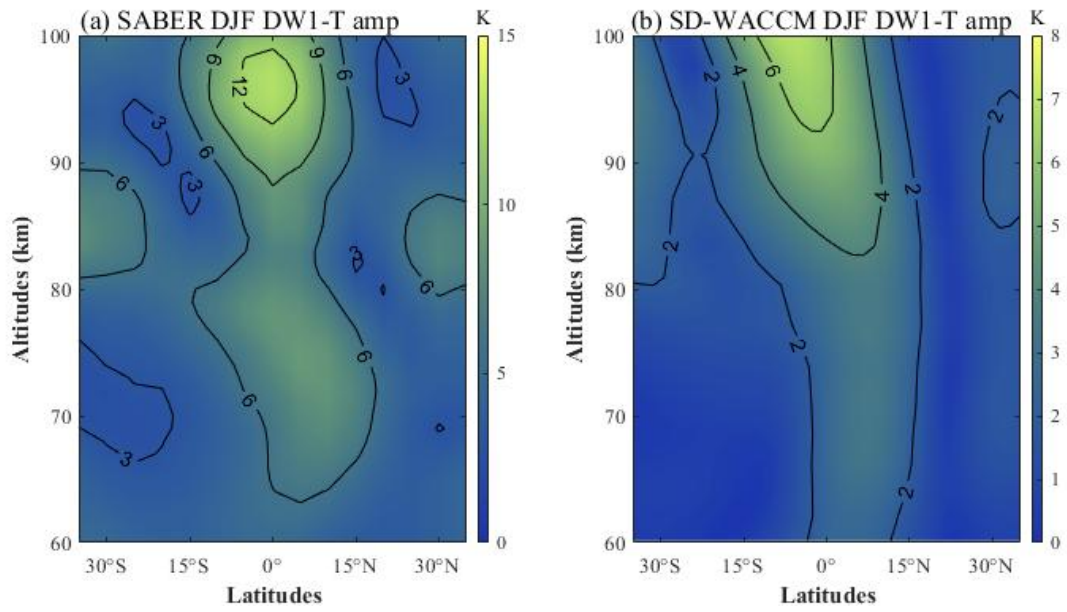
791 **Figure 8.** Correlation (a) between DW1 U and GW drag, (b) between DW1 U and GW forcing
792 from 1979 to 2014 winter (DJF). Solid lines and red shadings denote the positive responses, while
793 dashed lines and blue shadings denote the negative responses; the grey regions indicate where the
794 response is insignificant at the 95% level according to the F test.

795 **Figure 9.** The linear regression coefficient of normalized Niño3.4 in the GW forcing on the
796 amplitude of DW1-U during the 1979-2013 winters (DJF). Solid lines and red shadings denote the
797 positive responses, while dashed lines and blue shadings denote the negative responses; the grey
798 regions indicate where the response is insignificant at the 95% level according to the F test.

799

800

801 **Figures**

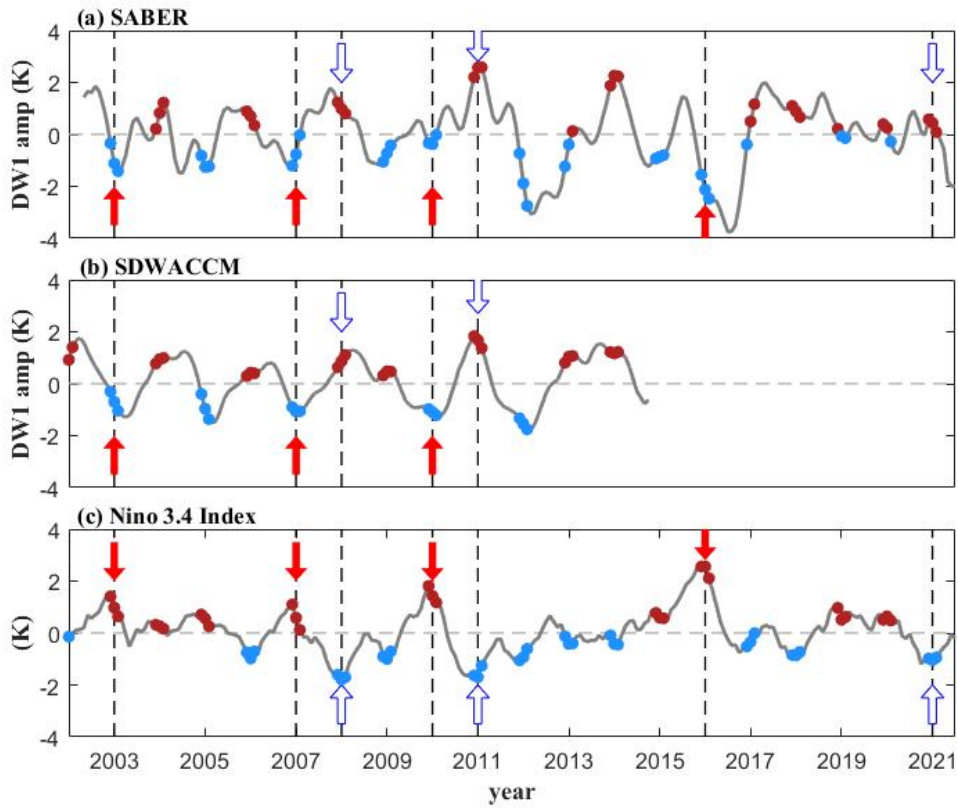


802

803 **Figure 1.** (a) The average DW1 temperature amplitude of SABER observation during the

804 2002-2013 winter (DJF, Dec-Jan-Feb). (b) the same as (a), but for SD-WACCM.

805

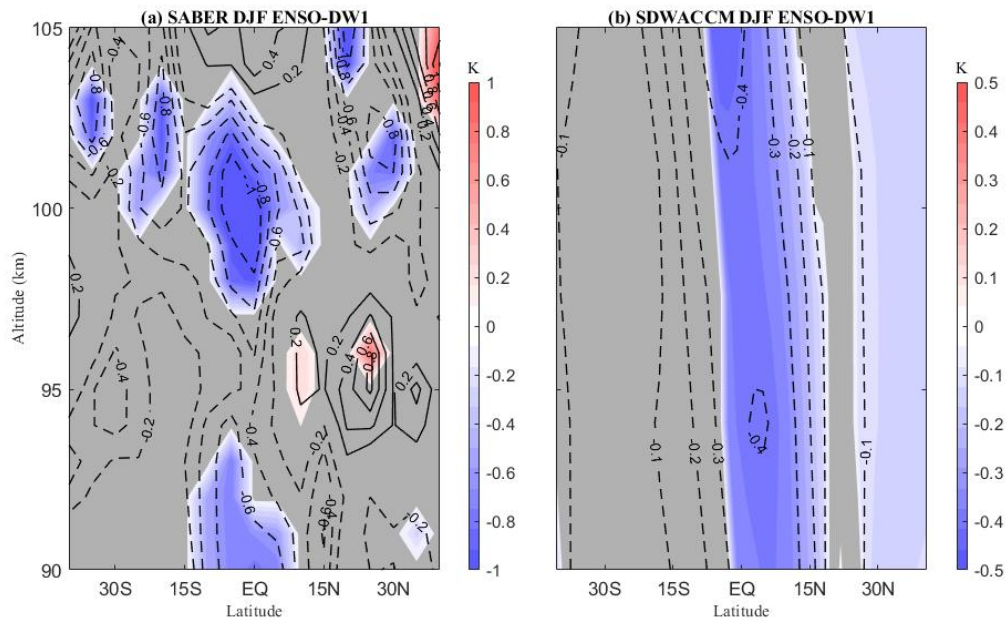


806

807 **Figure 2.** (a) The residual DW1 temperature amplitude of SABER observations averaged over
 808 10°S-10°N at 100 km from 2002 to 2021. (b) Same as in (a) but for SD-WACCM. (c) Niño3.4
 809 index. Dashed lines represent ENSO events. The red solid and hollow blue arrows denote the El
 810 Niño and La Niña events.

811

812



813

814 **Figure 3.** The linear regression coefficient of normalized Niño3.4 in SABER (a) and SD-WACCM

815 (b) winter DW1-T. The contour interval is 0.2 K for SABER and 0.1 K for SD-WACCM. Solid

816 lines and red shadings denote the positive responses, while dashed lines and blue shadings denote

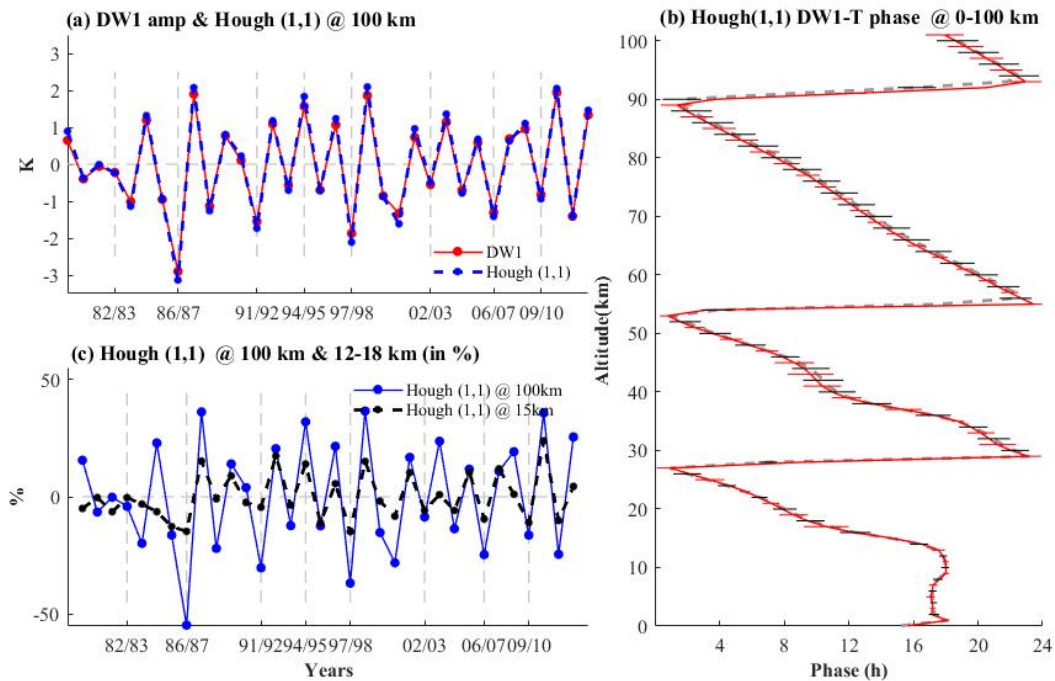
817 the negative responses; the grey regions indicate where the response is insignificant at the 95%

818 level according to the F test.

819

820

821



822

823 **Figure 4.** (a) The solid red line indicates the anomalous DW1 temperature amplitude of
 824 SD-WACCM simulations averaged over 10°S-10°N at 100 km during the 1979-2013 winter (DJF).

825 The blue dotted line indicates the Hough (1,1) mode of the DW1 temperature amplitude residual at
 826 100 km during the 1979-2013 winter (DJF). (b) The thin black dotted line indicates the Hough

827 (1,1) DW1-T phase of SD-WACCM simulations at 0-100 km during the 1979-2013 winter (DJF).

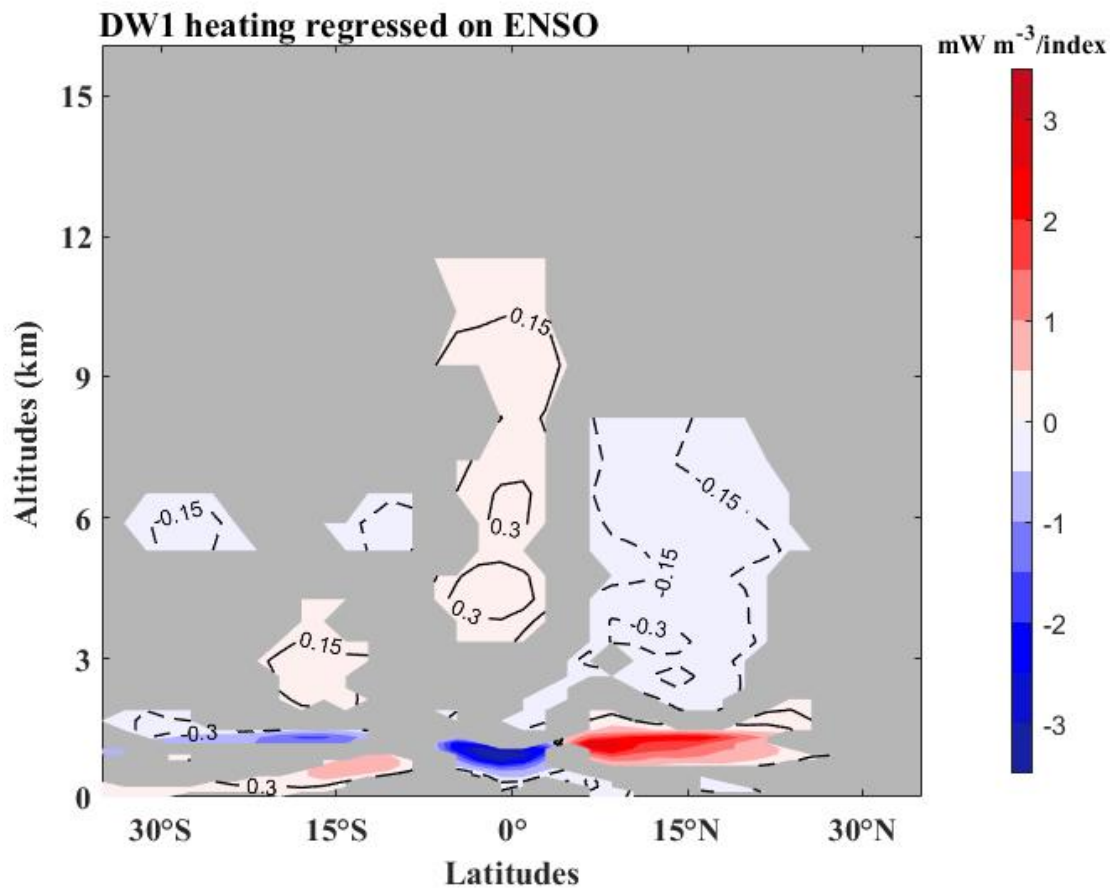
828 The thick black horizontal line indicates the standard deviation of the DW1-T phase. The solid red

829 line is the same but for El Niño winter. (c) The solid blue line is the same as in (a), and the black

830 dotted line is the same but for 15 km.

831

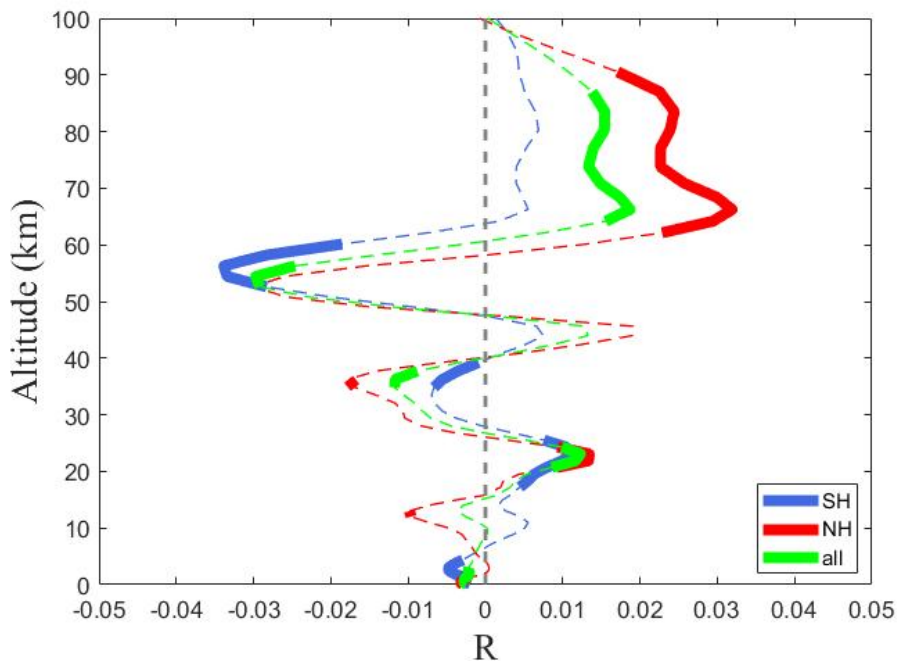
832



833

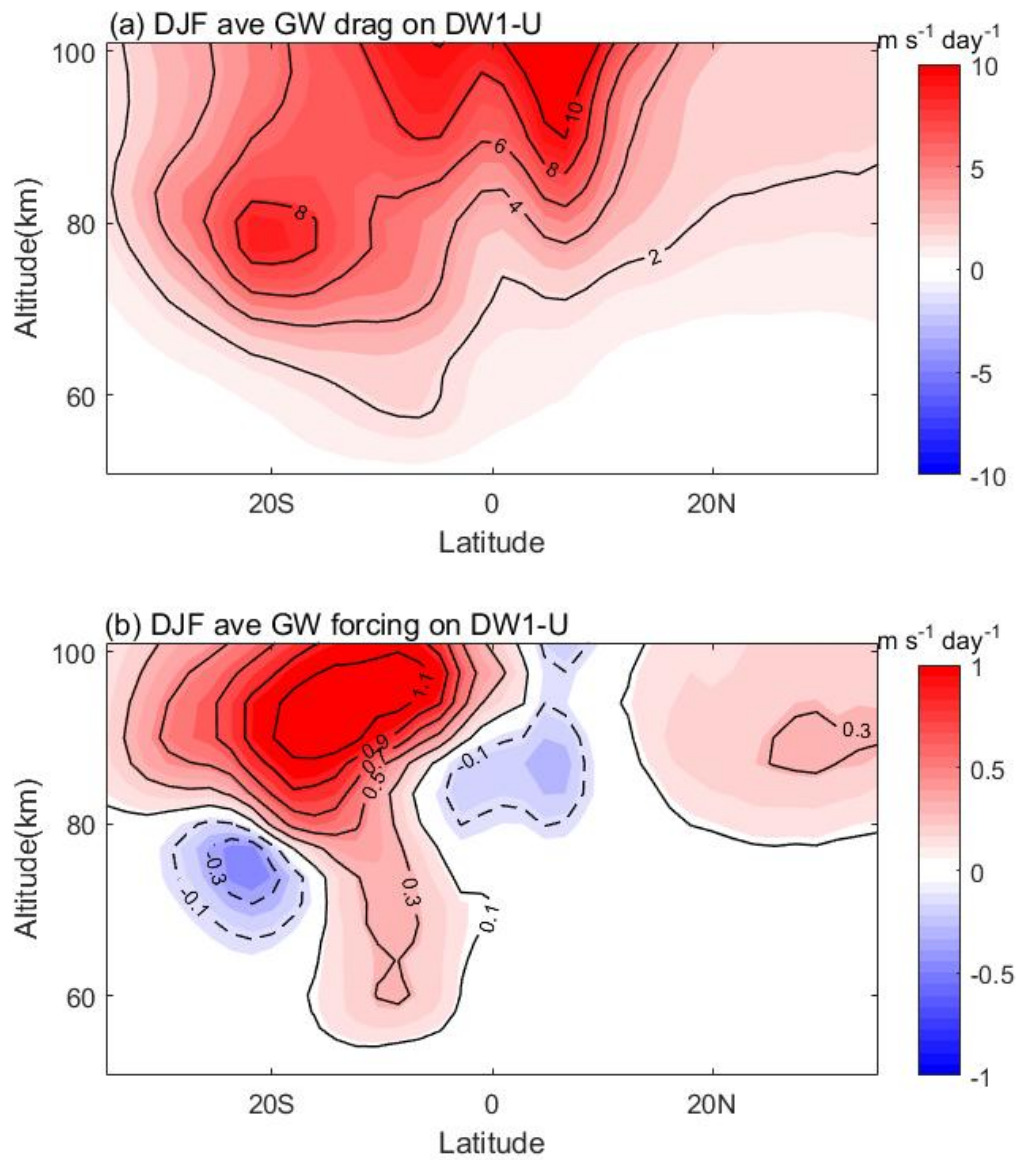
834 **Figure 5.** The linear regression coefficient of normalized Niño3.4 in SD-WACCM heating
 835 amplitude (mW/m^3 per index) during 1979-2013 winters (DJF). Solid lines and red shadings
 836 denote the positive responses, while dashed lines and blue shadings denote the negative responses;
 837 the grey regions indicate where the response is insignificant at the 95% level according to the F
 838 test.

839



840

841 **Figure 6.** The linear regression coefficient of normalized Niño3.4 in δR (the anomaly of the ratio
 842 of the absolute to planetary vorticity). The thin dashed red, blue, and green lines denote the
 843 averages of the Northern Hemisphere (from 15°N to 30°N), Southern Hemisphere (from 15°S to
 844 30°S), and the whole (15-30°N and 15-30°S), respectively. The thick, solid lines denote
 845 confidence levels higher than 95% for the F test.

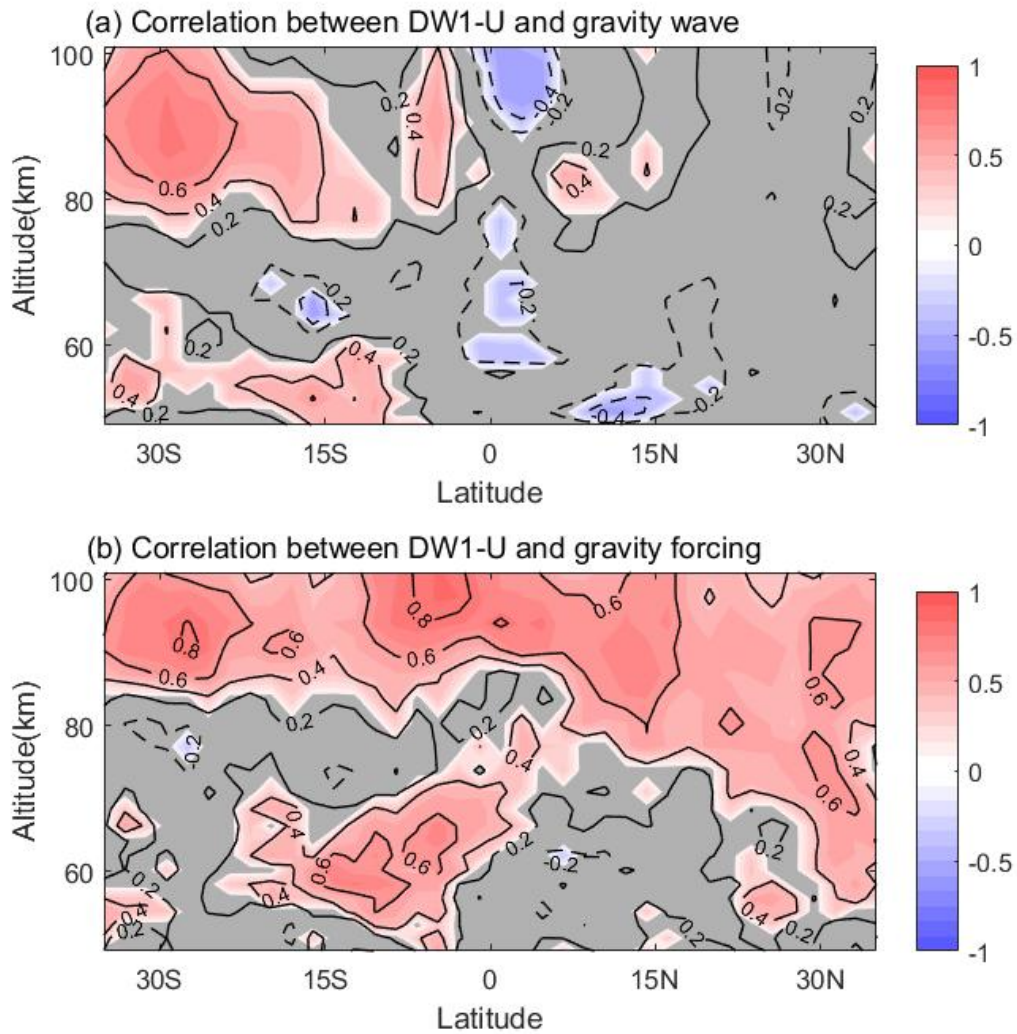


846

847 **Figure 7.** (a) Gravity Wave (GW) drag due to convection on the amplitude of DW1 tidal U during

848 the winter (DJF). (b) The same as (a), but for GW forcing.

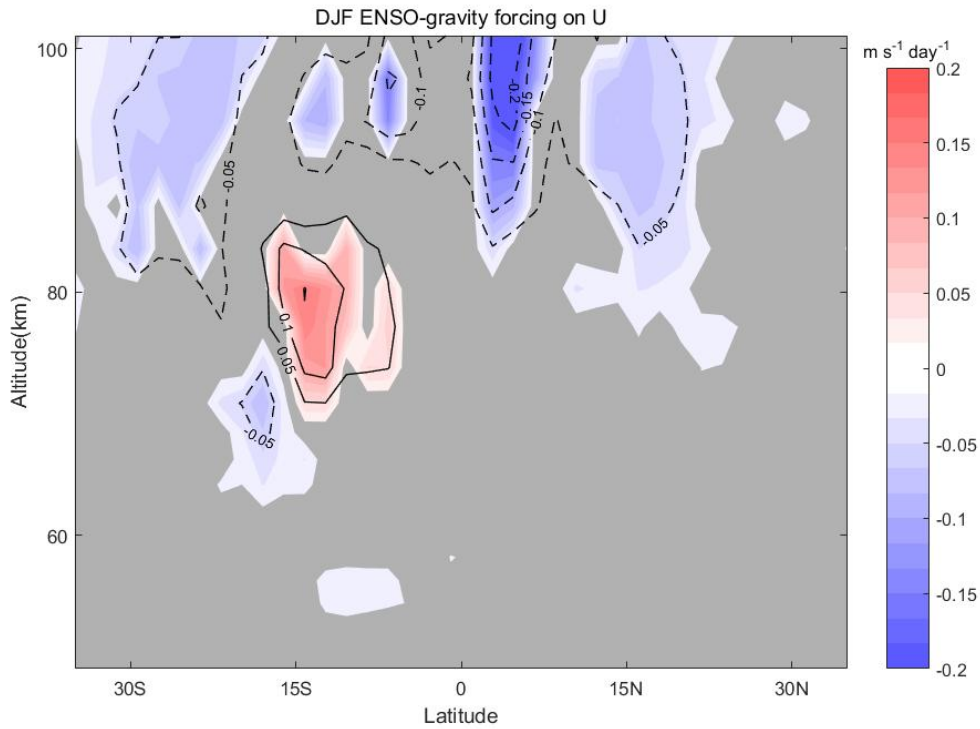
849



850

851 **Figure 8.** Correlation (a) between DW1 U and GW drag, (b) between DW1 U and GW forcing
 852 from 1979 to 2014 winter (DJF). Solid lines and red shadings denote the positive responses, while
 853 dashed lines and blue shadings denote the negative responses; the grey regions indicate where the
 854 response is insignificant at the 95% level according to the F test.

855



856

857 **Figure 9.** The linear regression coefficient of normalized Niño3.4 in the GW forcing on the
 858 amplitude of DW1-U during the 1979-2013 winters (DJF). Solid lines and red shadings denote the
 859 positive responses, while dashed lines and blue shadings denote the negative responses; the grey
 860 regions indicate where the response is insignificant at the 95% level according to the F test.